Journal of Saudi Chemical Society (2026) 30:63
https://doi.org/10.1007/s44442-026-00114-5

RESEARCH

One-step synthesis of magnetic tea waste biochar for efficient hexavalent chromium adsorption: process optimization, characterization, and adsorption mechanism

Shasha Guo[1,2] · Pan Wang[1,3] · Yao Zhu[1,4] · Yinyin Zhou[1,2] · Meiqin Li[1,4] · Xiao Lin[1,3] · Ping Xu[5] · Mufang Sun[1,4]

Received: 5 May 2026 / Accepted: 5 August 2026

Abstract

The booming global market for tea and new-style tea beverages has inevitably generated enormous quantities of waste tea residues, posing an urgent waste management challenge. Herein, spent tea leaves generated from tea beverage factory were employed as the precursor to synthesis N-doped magnetic biochar (NMTB) via one-step hydrothermal carbonization method with the modification by urea and $FeCl_3$. The adsorption performance of hexavalent chromium (Cr(VI)) of NMTB was better than pristine tea waste biochar. Furthermore, response surface methodology indicated that the best preparation temperature and time of NMTB were 200 °C and 4 h, respectively. The prepared NMTBs were characterized by SEM, BET, XRD, FTIR and XPS, showing the successful doping of N and Fe. Additionally, NMTB exhibited excellent Cr(VI) removal of 96.90%, with a maximum adsorption capacity of 63.03 mg/g. The adsorption process followed the Langmuir and pseudo-second-order models, suggesting that monolayer sorption and chemisorption dominated the adsorption process. Reusability performance demonstrated that the removal efficiency of NMTB remained at 84.49% after five times reuse, while the removal efficiency in real water sample test reached 96.55%. Moreover, mechanistic studies including FTIR and XPS investigation, zeta potential analysis, quantitative chromium speciation and density functional theory calculations demonstrated that the adsorption is dominated by electrostatic attraction, surface reduction and subsequent surface complexation. The study demonstrated that tea waste-derived magnetic biochar is an effective and regenerable material for Cr(VI) remediation. Moreover, it provides a sustainable strategy for upcycling waste tea residues from the rapidly expanding tea beverage industry, exemplifying a promising value-added approach for environmental remediation.

Keywords Spent tea leaves · Magnetic biochar · Nitrogen modification · Hydrothermal carbonization · Adsorption mechanism

✉ Shasha Guo
gss0620640@zju.edu.cn

✉ Ping Xu
zdxp@zju.edu.cn

✉ Mufang Sun
xynzsmf@163.com

[1] College of Tea Science, Henan Key Laboratory of Tea Plant Comprehensive Utilization in South Henan, Xinyang Agriculture and Forestry University, Xinyang, Henan 464000, China

[2] Dabie Mountain Laboratory, Xinyang, Henan 464000, China

[3] Henan Engineering Technology Research Center for High-Value Utilization of Waste Tea Resources in Tea Garden, Xinyang, Henan 464000, China

[4] Henan Provincial Engineering Research Center of Tea Processing and Inspection Research Center, Xinyang, Henan 464000, China

[5] Institute of Tea Science, Zhejiang University, Hangzhou, Zhejiang 310058, China

Published online: 19 August 2026

1 Introduction

Heavy metals are non-biodegradable and can persist for extended periods in soil, water and sediments for several decades [1]. These heavy metals are intensively used in human activities, such as industrial emissions of wastewater and waste residues from mining, smelting and electroplating; agricultural practices involving low-quality fertilizers and sewage irrigation; as well as certain hazardous household waste [2]. Through bio-accumulation and bio-magnification, heavy metals can be absorbed by human bodies, where their toxicity can cause damage to multiple organs, lead to neurological disorders and induce cancers [3]. Hexavalent chromium (Cr(VI)), primarily originating from industrial activities, exhibits high mobility and can create inflammation, cancer, and even death [4]. Currently, adsorption, ion exchange, membrane separation and several other technologies have been reported for treating heavy metal contamination [5, 6]. Adsorption is a promising strategy for wastewater treatment due to its cost-effectiveness, environmental friendliness and high efficiency. Therefore, affordable and renewable adsorbent is intended to be identify for Cr pollution control.

Biochar is a carbonaceous adsorbent with the advantages including low cost, readily available feedstocks and good adsorption, hence it has attracted much attention. Generally, biochar differs in specific surface area, pore distribution and other physicochemical properties because the different preparation conditions, such as the method of the preparation, the time and temperature of the reaction, and the additives used in the reaction [7, 8]. Hydrothermal carbonization (HTC) is a preparation method that converts the biomass into biochar at a lower temperature (180–280 °C) in comparison to pyrolysis. Moreover, HTC method does not require the raw materials to be pre-dried, which can save intensive energy when treating high-moisture feedstocks and has been widely applied for value-added utilization of waste, such as algal biomass [9]. Study was investigated about the properties of biochars derived from sycamore tree produced by HTC and slow pyrolysis (SP), respectively [10]. The results demonstrated that the yield of biochar by HTC is higher than by SP, and that it has a superior adsorption capability of Cr(VI). Besides, Li and Jin [11] compared the HTC and SP methods for the biochar production, and found that HTC produced biochar with a minimum price compared to SP process, holding a 71.8% probability of being the preferred option. Recently, Fe (iron) loaded modified biochar has been applied for heavy metal removal, showing excellent adsorption capability of Cr(VI) [12]. For example, magnetic biochar was synthesized by loading $FeCl_3$ onto agar biomass, and it contributes to elevate the removal performance of Cr(VI) [13]. Biochar produced from raspberry stalks and modified by Fe and urea showed higher efficiency of removal of Cr(VI) than original biochar [14]. Thus, an ideal strategy of modifying biochar with Fe and N to improve the adsorption of Cr(VI) warrants consideration. However, the existing literature on biochars still presents several critical deficiencies that limit their practical application for Cr(VI) removal. For instance, most studies rarely compared biochars under different preparation temperature and time, neglecting their effects on the resulting material properties. Besides, the synergistic co-doping of Fe and N combined with one-step HTC has rarely been investigated, despite its potential to introduce multifunctional active sites. This lack of correlation analysis between processes and performance significantly motivated the design and targeted optimization of tea waste-derived adsorbents.

Tea, a prevalent beverage all over the world, has long been associated with various health benefits. The Chinese tea market has generated nearly 107 billion U.S. dollars in 2023, and are expected to arrive at 179.4 billion U.S. dollars in 2029 (https://www.statista.com). Recently, the new-style tea beverages, which are typically prepared by blending raw tea leaves or infusions with fruits, vegetables, dairy, and other functional ingredients to meet contemporary consumer demands for flavor, health, and novelty, have become a regular indulgence for many consumers [15]. It is estimated that by 2028, the new-style tea beverage market size in China alone will exceed 400 billion yuan. However, this rapid expansion has inevitably been accompanied by the massive generation of spent tea leaves (STL), including those discarded from tea beverage extraction, instant tea manufacture, and household consumption. These huge amounts of organic agricultural waste can lead to secondary pollution and resource loss. From a solid waste value-added perspective, STL represent a promising carbonaceous precursor owing to their abundance, low cost, and inherently porous structure. Converting STL into biochar for heavy metal removal has therefore attracted increasing research attention. Several studies have demonstrated the feasibility of using tea waste-derived biochars to adsorb heavy metals from aqueous solutions [5, 16, 17]. Nevertheless, the Fe-N co-doping into tea waste-derived biochar and its targeted application for Cr(VI) alleviation has rarely been reported. Herein, we propose a strategy that directly valorizes STL into a Fe-N co-doped magnetic biochar (NMTB) via a one-step HTC route. Specifically, we optimized the HTC temperature and time through response surface methodology (RSM), and also overcame the limitation of single modification methods by introducing simultaneous Fe and N doping. Moreover, the Cr(VI) removal mechanism was elucidated by combining kinetic, isotherm, spectroscopic analyses, quantitative detection of Cr species and density functional theory (DFT). The selection of STL as the precursor not

only contributes to mitigating tea waste burden, but also embodies a circular economy concept. This work will provide a simple and efficient method of preparing adsorbents for Cr(VI), while also offering a promising approach to address the issue of tea residue waste.

2 Materials and methods

2.1 Materials

Tea waste used as the raw material of the biochar in this study were kindly supplied by a tea beverage manufacturer in Xinyang City, Henan Province, China (August, 2025). Specifically, after undergone the extraction and filtration processes at the beverage factory, the mixture of spent green and black tea leaves were collected as the raw material. The as-received wet STL were washed with deionized water to remove dust and surface impurities, and then air-dried under ambient conditions for 48 h to remove excess free water and facilitate grinding. The drained STL were subsequently ground into a fine powder (40 mesh) and used in the HTC process. Additionally, the farmland surface water sample was collected from Xinyang City, Henan Province (32°15′ N, 114°12′ E). All the chemical reagents including ferric chloride hexahydrate ($FeCl_3$), urea, zinc chloride ($ZnCl_2$), potassium dichromate ($K_2Cr_2O_7$), 1,5-diphenylcarbazide (DPC), acetone, hydrochloric acid (HCl), and sodium hydroxide (NaOH) were all at analytically pure grade (Sinopharm Chemical Reagent Co., Ltd., Shanghai, China) and used as received. Besides, the preparation of Cr(VI) standard solutions, chromogenic agents and pH regulators were provided in Text S1.

2.2 Preparation and modification of tea waste biochars

One-step HTC method was employed to prepare STL-derived biochars (TB). In brief, the 150 mL deionized water was mainly mixed with 5 g STL powder and 5 g zinc chloride ($ZnCl_2$, for pore-forming) to obtain pristine TB (pTB). For nitrogen (N)-doped TB (NTB) preparation, 150 mL 5% urea solution was used to replace the deionized water. Furthermore, 5 g STL powder, 5 g $FeCl_3$ and 5 g $ZnCl_2$ were added into 150 mL urea solution (5%) to perform N and Fe co-doped TB (N-doped magnetic TB, NMTB). That is, the STL powder was blended with $ZnCl_2$, urea and/or $FeCl_3$ at a 1:1 ratio, which is based on a review of previous reports and is a standardized parameter to maintain methodological consistency [18–20]. These mixtures were thoroughly stirred to dissolved and ultrasonicated for 30 min to disperse the powder homogeneously in the solution. Afterwards, the suspension was transferred into the reaction vessel, heated at 200 °C for 12 h. Subsequently, the reactor was cooled to ambient temperature, and the production was filtrated and washed to neutral with deionized water. These biochars were finally obtained after dried at 60 °C in the oven, and collected for further analysis.

Moreover, RSM experiment was designed to investigate the HTC preparation method of NMTB production. Central composite design (CCD) was employed as the tool for RSM design to obtain proper parameters of preparation of NMTBs. Temperature and time of preparation were chosen as independent parameters, and the design response values were expressed as the specific surface area and the percentage of Cr(VI) removal. Ranges of factors are chosen by taking into account prior relevant efforts. The reaction temperature was designed in the range of 180–220 °C, while retention time was varied at 4–18 h. The face-centered design element was chosen. The total number of the experiment is 11, which consists of 2 independent process variables, 4 factorial points, 4 axial points, and 3 replicates at the central points.

2.3 Batch adsorption of Cr(VI) by biochars

The batch adsorption experiment was carried out to evaluate the adsorption capacity of tea waste biochars for Cr(VI) under the effects of biochar dosage, initial concentration of Cr(VI), contact time and pH of Cr(VI) solution. Briefly, 0.05 g biochar was added into 50 mL, 50 mg/L Cr(VI) solution at pH = 2. Batch adsorption conditions were as followed: the biochar dosage was in the range of 0.02–0.5 g, the initial concentration of Cr(VI) was 10–200 mg/L, the contact time was 0.5–12 h, while the pH of Cr(VI) solution was adjusted from 2 to 7 by 0.1 mol/L HCl or NaOH solution. The mixture was shaken with a constant speed of 200 r/min for 6 h at the temperature of 303 K. After that, the solution was collected through 0.22 μm filtration membrane, and its concentration was determined by colorimetric method [6]. The standard curve was shown in Fig. S1. The adsorption capacity and removal efficiency were calculated by the formulas below (Eq. (1) and Eq. (2)):

$$q_e = \frac{(C_0 - C_e) \times V}{m} \tag{1}$$

$$R = \frac{C_0 - C_e}{C_0} \times 100 \tag{2}$$

Where C_0 and C_e are the initial and equilibrium concentrations (mg/L) of the solution, V (L) is the volume of the solution, m (g) is the mass of the biochar, q_e (mg/g) is the

equilibrium adsorbed amount, and R (%) represents the removal efficiency.

The isotherm data were fitted to the nonlinear Langmuir (Eq. (3)) and Freundlich (Eq. (4)) models.

$$q_e = \frac{q_m K_L C_e}{1 + K_L C_e} \tag{3}$$

$$q_e = K_F C_e^{1/n} \tag{4}$$

Where K_L (L/mg) is the Langmuir constant, q_m is the maximum adsorption capacity, K_F and n are the Freundlich constants, respectively.

The kinetic data were fitted to the nonlinear forms of the pseudo-first-order (PFO, Eq. (5)) and pseudo-second-order (PSO, Eq. (6)) models.

$$q_t = q_e \left(1 - e^{-k_1 t}\right) \tag{5}$$

$$q_t = \frac{k_2 q_e^2 t}{1 + k_2 q_e t} \tag{6}$$

Where, q_t (mg/g) is the adsorbed amounts at time t, while k_1 and k_2 are the rate constants of PFO and PSO, respectively.

All the nonlinear regressions were performed using the Levenberg–Marquardt iteration algorithm in Origin (version 2024). The goodness of fit was evaluated using the adjusted coefficient of determination (R^2_{adj}), the residual sum of squares (SSE) and the chisquare (χ^2).

2.4 Characterization of tea waste biochars

Biochars were characterized by N_2 adsorption/desorption isotherms to determine the Brunauer-Emmett-Teller (BET) specific surface area (SSA), total pore volume and average pore diameter with a MicrotracBEL-BELSORP MAX II analyzer (Japan). The surface morphology was analyzed with a scanning electron microscopy (SEM, ZEISS-GemeniSEM 360, Germany). Elemental composition of the biochars was analyzed using an energy-dispersive X-ray spectroscopy (EDS) detector (Oxford UltimMax40, British). The crystalline phases were estimated by X-ray diffraction (XRD) analysis (Bruker D8 Advance, Germany). The surface functional groups were probed by Fourier Transform Infrared Spectroscopy (FTIR, SHIMADZU-IRTracer 100, Japan), and the chemical composition was quantified by X-ray Photoelectron Spectroscopy (XPS) measurement (Thermo Fisher-ESCALAB 250Xi, USA). The concentration of total Cr in the solutions after adsorption and the Fe leaching contents were determined by Inductively Coupled Plasma Optical Emission Spectrometry (ICP-OES, Agilent 5800, USA).

3 Results and discussion

3.1 Comparative analysis of pTB, NTB and NMTB

3.1.1 Characterization of pTB, NTB and NMTB

The morphology of pTB, NTB and NMTB detected by SEM were displayed in Fig. 1a. Obviously, rare significant pore structure can be found in pTB and its surface is relatively dense and smooth, suggesting that cellulose structure of STL has been preserved. However, the SEM images of NTB and NMTB showed significant porous structure, roughness surface and plentiful biochar spheres, which could be attributed to the modification of urea and $FeCl_3$. The decomposition of urea and $FeCl_3$ with biomass materials under thermal condition produced gases and hence promoted the formation of pores. Besides, large amounts of iron oxide particles were loaded onto the surface of the biochars, which is in favor of the SSA of biochars [21]. It can be seen from the BET specific surface area results (Table 1) that pTB enlarged the SSA to 7.185 m^2/g from 4.880 m^2/g (raw material). Furthermore, NTB and NMTB all improved the SSA to 21.811 and 21.335 m^2/g, which prominently exceeded that of pTB. Meanwhile, total pore volume increased to 0.086 (NTB) and 0.074 cm^3/g (NMTB) compared to 0.031 cm^3/g (pTB). These results revealed that urea and $FeCl_3$ modifications are valid means for improving the pores' physical properties of biochar [22].

XRD is mainly used to explore the crystal structure and phase analysis of the material. The biochar samples were tested and analyzed by XRD, as shown in Fig. 1b. Both pTB and NTB possessed two broad peaks at 2θ around 22.6° and 43°, corresponding to the (002) and (100) crystal planes, which illustrated that both biochars had an amorphous structure. The two peaks of NTB have shifted due to the N doping. In addition, the XRD analysis of NMTB revealed that diffraction peaks at 2θ around 18.1°, 30.2° 35.5°, 42.7°, 46.7° and 62.9° can be assigned to Fe_3O_4 (Magnetite, PDF#75-0449), while the peaks at 24.9° and 32.4° can be ascribed to Fe_2O_3 (Hematite, PDF#33-0664) [23]. This also confirms that Fe had been successfully introduced on the tea waste biochar.

FITR spectra presented in Fig. 1c revealed similar characteristic peaks of three biochars on their surface. The broad peak at around 3320–3340 cm^{-1} represented the O–H stretching of the biochars can be observed in all three biochars [24]. The strong double peaks appearing at 2920 cm^{-1} and 2850 cm^{-1} characterized the antisymmetric and symmetric stretching vibrations of the C–H bonds in saturated alkyl group (methylene group, $–CH_2–$), indicating the incompletely carbonized aliphatic side chains remain in the HTC products [25]. Meanwhile, the peak at 1580 cm^{-1}

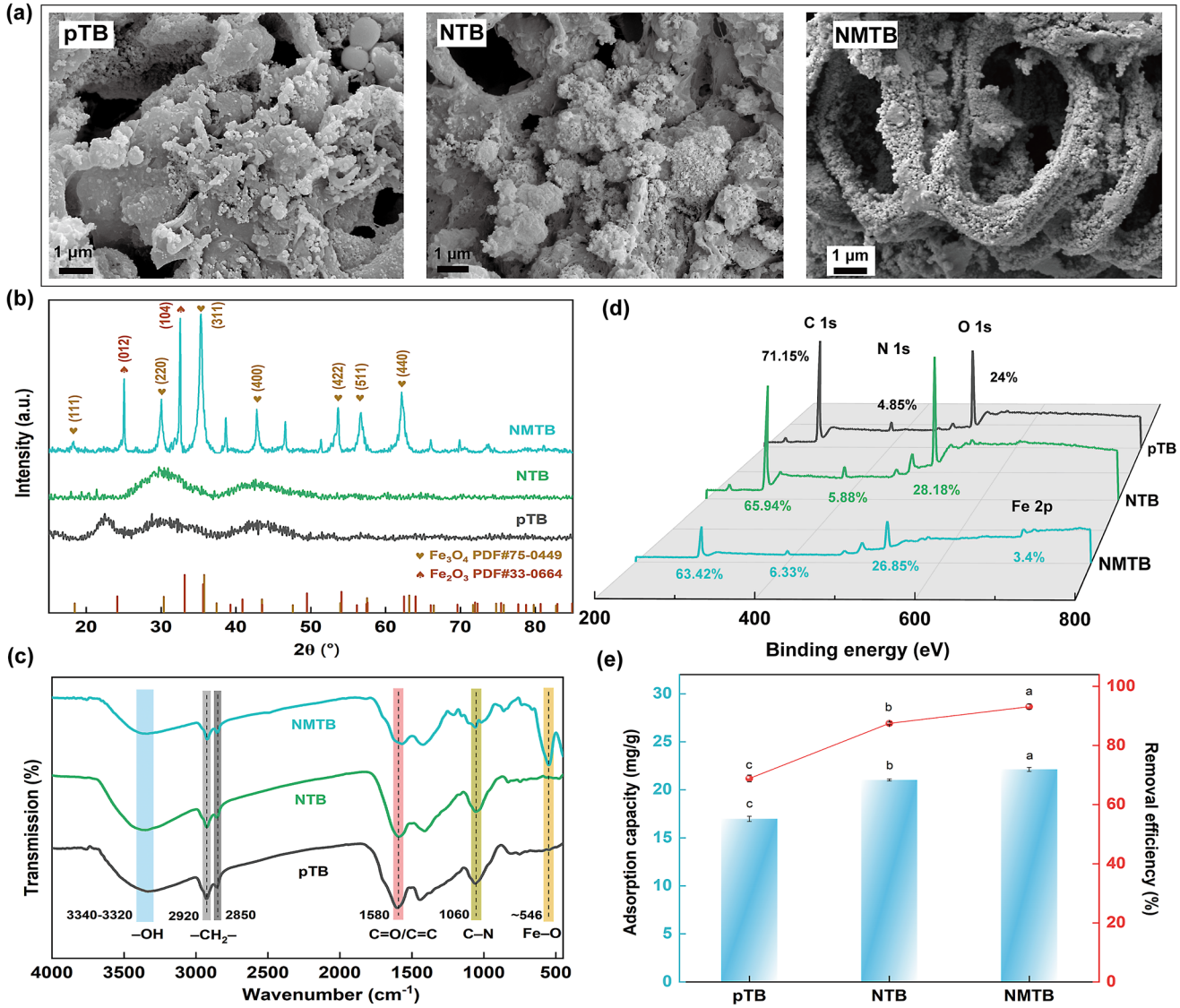

Fig. 1 SEM images (**a**), XRD (**b**), FTIR (**c**), XPS survey (**d**) and Cr(VI) adsorption performance (**e**) of different tea waste biochars. Different lowercase letters in (**e**) indicate statistically significant differences ($p < 0.05$) among tea waste biochars

Table 1 The pore structure parameters of tea waste biochars

Sample	Specific surface area (m^2/g)	Total pore volume (cm^3/g)	Average pore diameter (nm)
Raw material	4.880	0.017	9.299
pTB	7.185	0.031	17.069
NTB	21.811	0.086	15.683
NMTB	21.335	0.074	8.012

corresponded to C=O/C=C stretching vibration and slight shifting toward the lower frequency band occurred in NTB and NMTB compared to pTB may attributed to the doping of N and Fe. Furthermore, the peak at 1060 cm^{-1} ascribed to the C–N stretching vibration had greater intensity in NTB than pTB, suggesting the successful introduction of N [26]. Obviously, a strong adsorption peak at around 546 cm^{-1} found only in NMTB was corresponded to the Fe–O stretching vibration, which implying that $FeCl_3$ modification mainly supplied the formation of Fe–O group for NMTB [27]. FTIR analysis revealed the successful doping of Fe and N elements onto the surface of the biochars.

The XPS technique elucidated the surface elements variations of tea waste biochars in Fig. 1d. As can be found clearly from the XPS spectra, peaks at around 285, 401 and 532 eV represented C, N, and O, respectively on the biochars surface, while peak at around 710 eV represented Fe on the surface of NMTB. In addition, the modification of urea and $FeCl_3$ brought the change of element content on the biochars surface. The surface N content of NMTB (6.33 at.%) was highest, followed by NTB (5.88 at.%) and pTB

(4.85 at.%), suggesting the successful doping of N after urea modification. Meanwhile, the Fe content of NMTB was 3.4 at.%, while its C content decreased and O content increased compared to pTB. This implied that the modification introduced Fe and increased O-containing functional groups in NMTB. Therefore, N and iron had been loaded on the surface of tea waste biochar, indicated the successful incorporation of N and Fe into the carbon skeleton [28].

3.1.2 Adsorption performance of pTB, NTB and NMTB

The adsorption performance of pTB, NTB and NMTB for Cr (VI) were analyzed with 0.1 g adsorbent adding into 50 mL Cr(VI) solution (50 mg/L, pH = 2) for 24 h. The results in Fig. 1edemonstrated that the pTB, NTB and NMTB showed significant differences ($p < 0.05$) of adsorption amounts and removal efficiencies, suggesting their different adsorption performance of Cr(VI). Both the adsorption amounts and removal efficiencies followed the order NMTB > NTB > pTB. pTB possessed the lowest adsorption amounts at 19.44 ± 0.16 mg/g. Comparatively, NMTB showed the highest adsorption amounts of 22.13 ± 0.21 mg/g, representing an increase of 30.38%. The removal efficiencies increased from 68.83% (pTB) to 93.11% (NMTB), suggesting that the successful modification of pTB with N and Fe significantly enhanced its Cr(VI) adsorption ability. Comparable enhancements in Cr(VI) removal efficiency after magnetic modification have been reported for biochars derived from other agricultural residues [29]. Generally, the substantially improved adsorption performance of NMTB indicated that Fe and N dual doping offers greater advantages in the modification of tea waste biochar. Therefore, a more detailed study of NMTB was conducted subsequently.

3.2 RSM optimization for HTC preparation process of NMTBs

HTC preparation temperature and time can affect the properties and adsorption performance of NMTBs. Table S1 showed the outcomes of the preparation parameters optimization of NMTBs by RSM, while the analysis of variance (ANOVA) listed in Table S2 and S3 tested the significance of the fitted equations of SSA and removal efficiency, respectively. It can be seen that both two models exhibited very high level of significance (Model F-value were 37.85 and 32.94, respectively; $p < 0.01$), while the "Lack of fit F-value" were not significant ($p > 0.05$). Additionally, the difference between coefficient of determination ($R^2 = 0.9743$ and 0.9705, respectively) and R^2_{adj} (0.9485 and 0.9411, respectively) were less than 0.2 (R^2-$R^2_{adj} < 0.2$), which verified that both of the models were reliable. According to Fig. S2 and the F-value, the effect of the preparation temperature was more significant than the preparation time to both SSA and Cr(VI) removal efficiency. Therefore, preparation temperature is crucial important to the improvement of SSA, and also plays a key role in enhancing the removal efficiency of Cr(VI). Subsequent analysis of physicochemical properties and Cr(VI) adsorption performance in this study mainly focused on NMTBs with different HTC temperature at 4 h, and their labels were simplified as NMTB-180, NMTB-200 and NMTB-220. Furthermore, it should be noted that the present RSM optimization focused on the reaction conditions (temperature and time) during HTC process, while the dosages of $FeCl_3$, urea, and $ZnCl_2$ were fixed based on previous literature. Future studies will incorporate these variables into a more comprehensive multivariate optimization to further refine the material properties and performance.

3.3 Physicochemical properties of NMTBs

The specific surface area is one of the most crucial properties affecting the adsorption ability of biochar. NMTB-200 owned the highest SSA (25.177 m^2/g), followed by NMTB-180 (18.110 m^2/g) and NMTB-220 (14.591 m^2/g). The results demonstrated that increasing HTC temperature from 180 °C to 200 °C contributed to the improvement of SSA. However, further elevated HTC temperature may cause the collapse of pores, reducing the numbers of micropores and leading to the decrease of SSA [30, 31].

Furthermore, the SEM images displayed in Fig. 2a–c showed the surface morphology properties of magnetic biochars. NMTB-180 exhibited a typical fibrous structure of plant and limited pores and cracks (Fig. 2a). Comparably, NMTB-200 presented more, larger or deeper pores than NMTB-180, with the disappearance of the plant fibrous structure (Fig. 2b). The morphological changes can be well explained by the increase of HTC temperature from 180 °C to 200 °C. The framework of the STL was destroyed through the heating process, and the volatile compounds were released [32]. The roughness architecture is in favor of the improved SSA and the adsorption ability. However, at higher HTC temperature (220 °C), the collapse carbon skeleton of the biomass significantly blocks some pores, leading to a reduction in porous structure (Fig. 2c), hence resulted in the lower SSA of NMTB-220. Besides, the rough and irregular porous structures with numerous particles on the surface of magnetic biochars can be observed, representing that Fe particles have successfully adhered to the surface of the NMTBs materials [33]. The results suggested that the volatile compounds in biomass gradually leach out with the increase of HTC temperature, forming microporous and mesoporous structures of biochars, and leading to the increase of SSA. Fig. 2d–f presented the EDS elemental mapping results of NMTB-180, NMTB-200 and

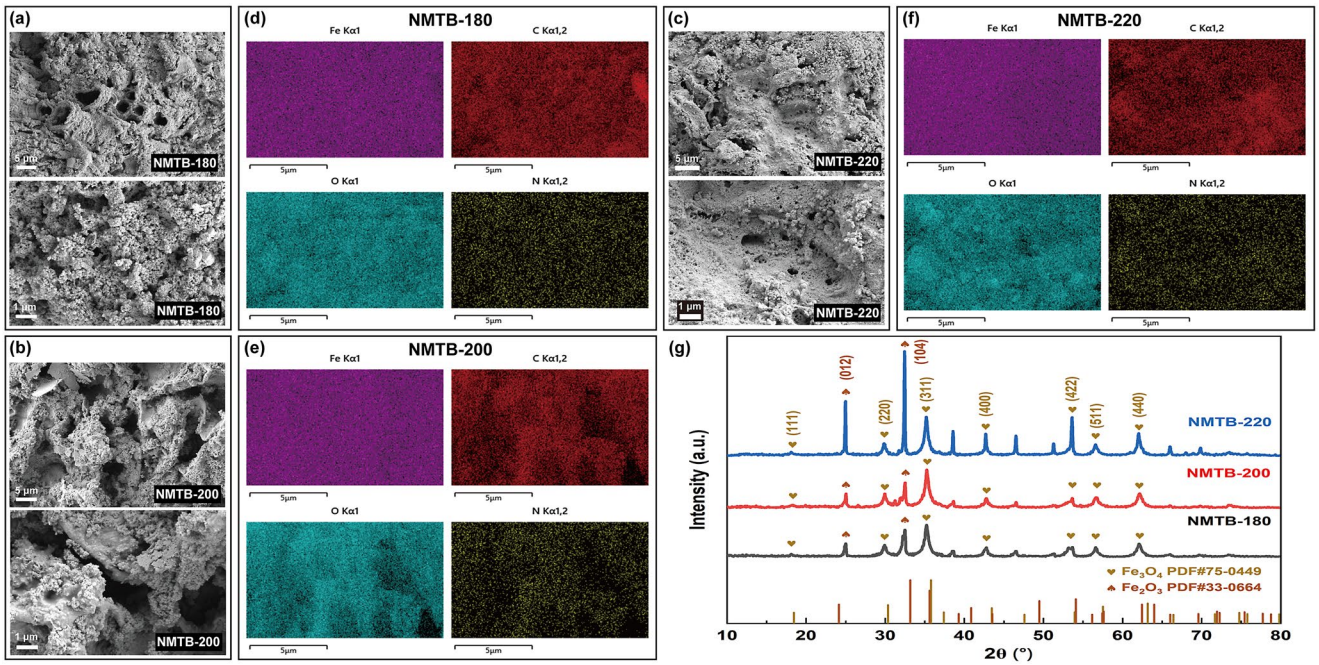

Fig. 2 SEM images of NMTB-180 (**a**), NMTB-200 (**b**) and NMTB-220 (**c**) At different magnifications, EDS mapping of Fe, C, O and N elements in NMTB-180 (**d**), NMTB-200 (**e**) and NMTB-220 (**f**), and XRD patterns (**g**) of NMTBs

NMTB-220. It illustrated that both Fe and N showed highly homogeneous distribution across the scanned area. No obvious iron-rich agglomerates or nitrogen-depleted regions are observed, confirming that the one-step HTC process successfully incorporates Fe and N species uniformly into the carbon matrix. The corresponding EDS elemental composition (Fig. S3a) further confirmed the presence of Fe and N with atomic contents of approximately 4.03–5.62 at.% and 4.95–5.37 at.%, respectively. In addition, approximately 2.63–3.38 at.% of Zn was detected on NMTBs (Fig. S3b), which may attribute to the residual $ZnCl_2$ poreforming agent used during HTC synthesis. Despite thorough washing, trace Zn may be retained due to complexation with surface functional groups or encapsulation within the carbon matrix.

The XRD analysis of magnetic biochars were depicted in Fig. 2g. From the XRD patterns of three magnetic biochars, the diffraction peaks emerged at around 2θ = 18.1°, 29.9°, 35.2°, 42.8°, 53.6°, 56.7° and 62.1° indexing to the (111), (220), (311), (400), (422), (511) and (440) lattice planes of Fe_3O_4, while the peaks at 24.9° and 32.4° were assigned to (012) and (104) crystalline planes of Fe_2O_3. It can be confirmed from these characteristic peaks that Fe was successfully doped onto the biochars surface with the formation of iron oxide. According to the diffraction files of Fe_3O_4 and Fe_2O_3, these diffraction peaks shifted to the left (towards lower angles), indicating an increase in the interplanar spacing. This increase may attribute to the doping of heteroatom (such as N atom in this study) onto the lattice [22]. Besides, the typical broad peaks which were attributed to graphite carbon were not observed from three magnetic biochars, suggesting that the cellulose of the pristine material might decomposed during the HTC process [34]. This phenomenon is benefit for the doping of Fe or N atoms by supplying a large amount of defect sites.

The vibrating scanning microscope (VSM) was performed to investigate the magnetic properties of NMTBs, with a field sweeping from − 10,000 to + 10,000 Oe. As illustrated in Fig. S4, the magnetic saturation (Ms) values of NMTB-180, NMTB-200 and NMTB-220 were 1.78, 2.98 and 5.95 emu/g, respectively, suggesting that the increasing HTC temperature is beneficial to the improvement of Ms. Additionally, the low Ms values of NMTBs possibly owing to the low crystallinity or the small crystal size of magnetite Fe_3O_4 generated during the magnetization of biochar [35].

3.4 Cr(VI) adsorption performance of NMTBs

3.4.1 Effect of biochar dosage on Cr(VI) adsorption

The effects of NMTB dosage, initial concentration of Cr (VI), the contact time of adsorption and pH values have been studied respectively and shown in Fig. 3. It can be observed in Fig. 3athat when the biochar dose increased from 0.02 g to 0.1 g, the removal percentages of Cr(VI) improved from 35.71%, 38.67% and 30.14% to 86.73%, 96.90% and 77.77% by NMTB-180, NMTB-200 and NMTB-220, respectively. With the further increase of biochar dose (to

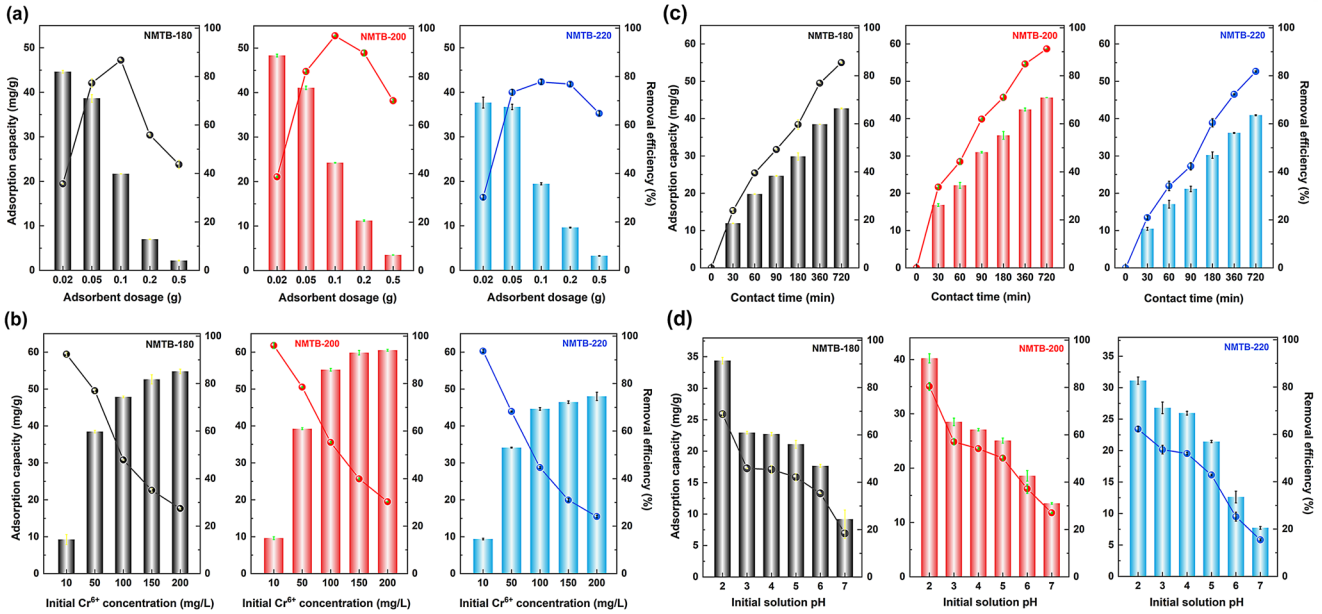

Fig. 3 The effects of biochar dosage (**a**), initial concentration of Cr(VI) (**b**), contact time (**c**) and initial solution pH (**d**) On Cr(VI) adsorption performance by NMTBs

0.5 g), the removal rates were all decreased. Meanwhile, the adsorption capacities were notably declined from 44.64, 48.33 and 37.68 mg/g to 2.18, 3.51 and 3.23 mg/g by NMTB-180, NMTB-200 and NMTB-220, respectively. This phenomenon is mainly because that when the biochars dosage is low, the surface functional groups supplied by magnetic biochars are relative less, and the Cr ions binding with the functional groups is more complete, resulting in the high adsorbent utilization and consequently high adsorption capacity. However, the initial Cr(VI) concentration is high (50 mg/L), the low dosage provides insufficient adsorbent sites in the adsorption system, leading to a low removal rate [36]. When the dosage of adsorbent is excessive, the dispersibility of the adsorbent in the solution is impaired, which illustrated that the total specific surface area of the adsorbent is increased. This leads to an incomplete adsorption by individual adsorbent particles. Consequently, the utilization rate of the adsorbent decreases, causing the rise of removal rate, while the adsorption capacity declines [37]. To facilitate a unified study of the adsorption behavior of the three magnetic biochars, 0.05 g was selected as the adsorbent dosages for subsequent research.

3.4.2 Effect of initial concentrations on Cr(VI) adsorption

The effect of different initial concentrations on Cr (VI) adsorption performance was analyzed in Fig. 3b. It was described that the initial concentration increased from 10 to 200 mg/L, the adsorption capacity enhanced from 9.23, 9.60 and 9.37 mg/g to 54.79, 60.53 and 48.01 mg/g by NMTB-180, NMTB-200 and NMTB-220, respectively. Meanwhile, the removal rates were declined remarkably. At low initial Cr(VI) concentrations, the adsorption sites on the magnetic biochars are plentiful, so the adsorption has not yet reached saturation. Therefore, the removal rates were high, but the actual adsorbed amounts remained low. As the concentrations elevates, the abundance of Cr ions rises, occupying a great number of the adsorption sites, resulting in the increase of adsorption capacity. However, the adsorption capacity will reach equilibrium when the adsorption sites are completely saturated, rather than continuing to increase, as the initial Cr(VI) concentration rises [38].

3.4.3 Effect of adsorption time on Cr(VI) removal

The adsorption capacities and removal rates at different adsorption time were investigated in Fig. 3c to describe the effect of contact time of NMTBs on Cr(VI). It can be seen that at the early period of the adsorption, the adsorption capacities and removal rates of three magnetic biochars were all at lower stage. As the reaction time increased, both removal efficiencies and adsorption capacities exhibited rapid growth. After 6 hours of adsorption, the increasing rate gradually leveled off as equilibrium was approached. It can be speculated that the biochar surface possesses numerous active adsorption sites at the initial adsorption stage, which enable the rapid and substantial uptake of Cr ions from the solution. As time progresses, an increasing number of adsorption sites become occupied by the Cr ions, resulting in the reducing number of available active sites.

Hence, the adsorption rate gradually slows down, eventually approaches equilibrium. Moreover, during the initial adsorption stage, the high concentration of Cr(VI) in the solution creates a significant adsorption driving force, leads to a rapid adsorption rate of Cr(VI). Nevertheless, as the adsorption proceeds, Cr ions compete for the remaining adsorption sites, causing the decrease of absorption amount [39].

3.4.4 Effect of pH on Cr(VI) adsorption

The pH of the solution is a pivotal parameter that affect the adsorption efficacy of biochar. As can be seen in Fig. 3d, it is evident that all NMTBs exhibits a decrease adsorption capacity and removal efficiency with the increase of pH value from 2 to 7. The maximum Cr(VI) uptake of NMTB-180 (34.38 mg/g), NMTB-200 (40.21 mg/g) and NMTB-220 (31.11 mg/g) achieved at pH = 2, corresponded with the highest removal efficiency of 68.75%, 80.42% and 62.22%, respectively. At mildly acidic conditions (pH 4–5), NMTBs still retained approximately 60% of its maximum capacity. Notably, a significant decrease of adsorption performance occurred as the solution pH increased to 6 and 7. This may be because, under acidic conditions, Cr(VI) exists primarily as $HCrO_4^-$ and $Cr_2O_7^-$, whereas as the pH increases, Cr(VI) exists primarily as CrO_4^{2-}. As reported previously, $HCrO_4^-$ has a higher adsorption free energy than CrO_4^{2-}, therefore is more readily adsorbed [40]. Besides, the concentration of OH^- in the solution gradually increases as the pH rises, leading to competitive adsorption with CrO_4^{2-}. In contrast, the abundance of protons and positively charged surface functional groups in acidic media enhances the electrostatic attraction between the chromium anion and NMTBs [41]. As the solution's pH increases, the number of protons and positively charged functional groups decreases, which may reduce the number of available reaction sites on the biochar and weaken the electrostatic attraction between the chromium anion and the biochar [42].

3.5 Adsorption isotherms and kinetics models

3.5.1 Adsorption isotherms of NMTBs

The Langmuir and Freundlich models were utilized for adsorption isotherms analysis on Cr (VI). Figure 4a showed the fitting curves of the adsorption isotherms of three magnetic biochars. It can be observed that the experimental data of NMTB-180, NMTB-200 and NMTB-220 were more fitted to Langmuir isotherm compared to Freundlich isotherm. Besides, the corresponding parameters listed in (Table S4) exhibited that the Langmuir R^2_{adj} values for NMTB-180, NMTB-200 and NMTB-220 (0.985, 0.968 and 0.973, respectively) were higher than the Freundlich R^2_{adj} values (0.834, 0.924 and 0.905, respectively). What's more, the Langmuir model of NMTBs exhibited the smaller SSE (3.435, 10.610 and 4.999, respectively) and χ^2 (17.176, 53.046 and 24.999,

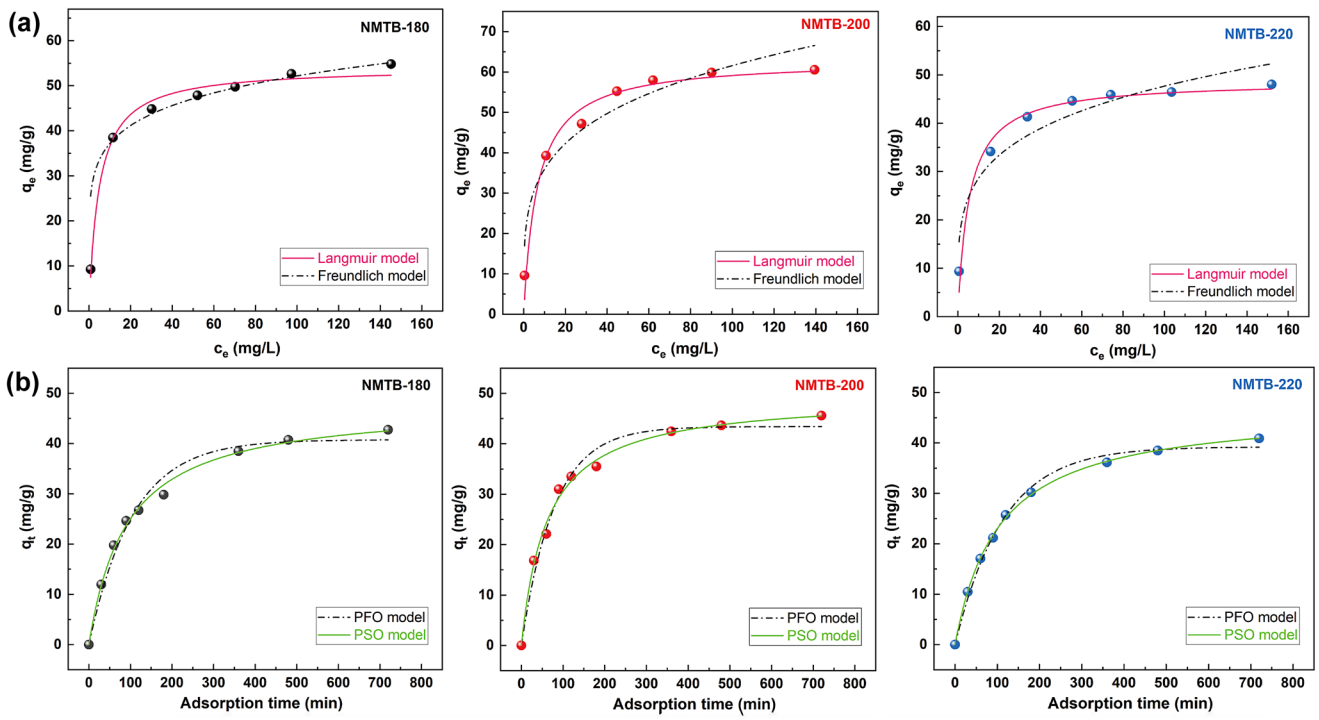

Fig. 4 Adsorption isotherms and the fitting curves by Langmuir and Freundlich models (**a**), adsorption kinetics and the fitting curves by PFO and PSO equations (**b**) For Cr(VI) adsorption by NMTBs. (m = 0.05 g, V = 50 mL, C_0 = 50 mg/L, pH = 2)

respectively) values than Freundlich model's (SSE: 7.692, 25.138 and 17.769; χ^2: 7676.629, 125.688 and 88.844, respectively). The above results suggested that the Langmuir model provides a more appropriate description of the Cr(VI) adsorption by NMTBs, with the monolayer sorption dominating the adsorption process, forming complexation interaction involving functional groups such as Fe–O and O–C = O bonds [43].

Moreover, q_m value calculated from Langmuir model (Eq. (3)) represented the maximum theoretical adsorption capacity, and NMTB-200 owned the highest q_m value for Cr(VI) (63.03 mg/g), followed by NMTB-180 (54.06 mg/g) and NMTB-220 (48.74 mg/g). The adsorption capacities of NMTB demonstrated that the magnetic biochars derived from STL possessed good adsorption for Cr(VI), while NMTB-200 shows the best adsorption ability in accordance with its SSA result. Previous studies have obtained various tea waste-based biochars with different Cr(VI) adsorption capacities, including 34.59 mg/g of used green tea leaves after consumption [44] and 38.62 mg/g of tea waste biochar [37], as well as biochars made from other pristine materials, such as the 21.3 mg/g of *Eucalyptus globulus* bark [45], 20.05 mg/g of cotton stalk [46] and 43.12 mg/g of sugarcane bagasse [47]. Certainly, numerous biochars reported before also contained higher Cr(VI) adsorption amounts [48]. Therefore, further modification on our tea waste-based magnetic biochars can be explored to enlarge their adsorption ability.

Additionally, R_L parameter obtained from the Langmuir model can be used to determine whether the adsorption of biochar is thermodynamically favorable, thereby characterizing its adsorption properties. Generally, $R_L = 0$ indicates irreversible adsorption, while $0 < R_L < 1$ suggests the adsorption process proceeds relatively easily and $R_L > 1$ expresses unfavorable adsorption [49]. As shown in Table S4, R_L of three NMTB were in the range of 0–1, demonstrating favorable adsorption of Cr(VI) by the magnetic biochars. Consequently, the N-doped magnetic biochars of STL prepared by HTC method can effectively adsorb Cr(VI), representing a low-cost, high-efficiency and environmentally friendly adsorbent material with significant application value.

3.5.2 Adsorption kinetics of NMTBs

Adsorption kinetics can describe the speed of the adsorption, and PFO and PSO models are the primary kinetics. The fitting results were showed in Fig. 4b and Table S5. According to the coefficient, the PSO R^2_{adj} values of NMTB-180, NMTB-200 and NMTB-220 were 0.996, 0.993 and 0.999, respectively. This is compared to the PFO R^2_{adj} values of 0.979, 0.980, and 0.993, suggesting that the PSO model fitted the experimental Cr(VI) adsorption data comparatively better than the PFO model. The error function analysis (SSE and χ^2 values) further supports the model selection. The PSO model yields lower SSE and χ^2 values compared with the PFO model among NMTBs, confirming its better fitting accuracy and indicating that the overall adsorption rate is controlled by chemisorption. It has been reported that the PFO model usually describes the initial stage of adsorption well, and is often associated with a physisorption-dominated process, whereas the PSO model usually implies that the overall rate is limited by sites of chemisorption [50, 51]. Nevertheless, although the PSO model better fits the adsorption process of NMTBs, it cannot conclusively prove chemisorption. Therefore, additional characterization and theoretical analyses are required to establish the underlying mechanism, which are discussed in detail in Sect. 3.7.

Moreover, the q_e of Cr(VI) adsorption calculated from the PSO model were 47.91, 49.42 and 46.81 mg/g of NMTB-180, NMTB-200 and NMTB-220, respectively, which were closer to the experimental data than the q_e values from the PFO model (40.76, 43.41 and 39.23 mg/g, respectively). Among them, NMTB-200 has the best Cr(VI) adsorption performance than NMTB-180 and NMTB-220. Based on the adsorption curves, NMTB-200 exhibits a faster increase in Cr(VI) adsorption capacity compared to NMTB-180 and NMTB-220. Therefore, NMTB-200 offers the advantages of possessing a higher Cr(VI) adsorption capacity and achieving adsorption equilibrium faster than NMTB-180 and NMTB-220, making it a promising candidate adsorbent for removing Cr(VI) while also addressing the issue of wasting tea residue resources.

3.6 Reusability, environmental remediation potential and performance comparison analysis

In order to verify the adsorbent recyclability and reusability performance, 0.1 g NMTB-200 was used for 50 mg/L Cr (VI) solution (50 mL) adsorption for 24 h, and then was desorbed by 0.1 mol/L NaOH solution for 2 h. The recycle was conducted for five times and each of the removal performance was displayed in Fig. 5a. As can be seen, after five adsorption-desorption cycles, the removal rates of NMTB-200 decreased from 99.95% to 84.49%, suggesting a low reduction in the efficiency of Cr (VI) removal. The results indicate that NMTB possesses excellent reusability and is a highly promising and cost-effective adsorbent for Cr(VI). Besides, ICP-OES was applied for the concentration of Fe leaching. The results showed in Fig. 5b indicated that the dissolved Fe concentrations in all five cycles were low (less than 1.32 mg/g), indicating that NMTB-200 effectively suppressed Fe leaching and enhanced structural stability. Moreover, the Fe concentrations in the desorption solutions were decreased from 1.32 to 0.07 mg/L, which may illustrate that

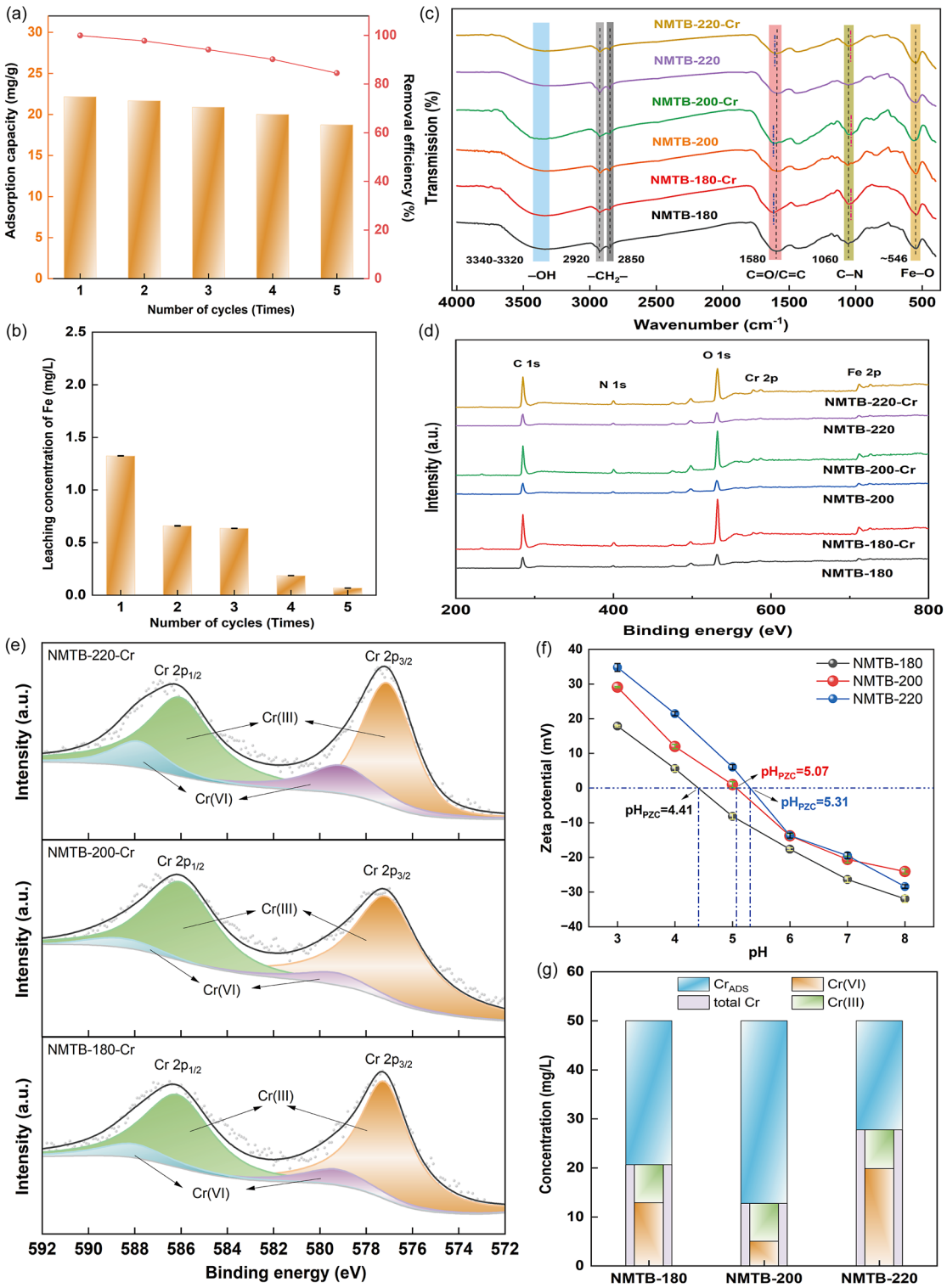

Fig. 5 The effects of cycle number on Cr(VI) adsorption performance by NMTB-200 (**a**), leaching concentration of Fe in different cycles of desorption solutions (**b**), FTIR (**c**) and XPS (**d**) spectra of NMTBs before and after adsorption, Cr2p spectra of NMTBs after adsorption (**e**), zeta potential plots and pH_{PZC} of NMTBs (**f**), and Cr(VI), Cr(III), total Cr and Cr_{ADS} concentrations of NMTBs. Cr_{ADS} represented concentration of adsorbed Cr on the solid phase, which was calculated by 50 (mg/L) minus total Cr (mg/L)

a small fraction of weakly bound or surface-exposed iron species was removed during the first desorption, while the iron deeply embedded in the carbon matrix remains tightly anchored and resistant to further leaching. The consistently low iron release demonstrates that the Fe species are tightly anchored within the carbon matrix, likely due to the encapsulation by the hydrothermal carbon layer and the formation of stable Fe–N and Fe–O bonds, which prevent significant dissolution even under the alkaline desorption conditions [52].

In addition, 0.1 g NMTB-200 was also tested to adsorb real surface water sample from the farmland. The water sample was collected from an agricultural drainage ditch where low Cr(VI) contamination risk has been previously detected, reflecting realistic field exposure levels in soil-water systems. The Cr(VI) concentration of the collected sample was 0.0454 mg/L, which falls between the Class I (<0.01 mg/L) and Class II (<0.05 mg/L) water quality standard values. After 24 h adsorption, the Cr(VI) concentration decreased to 0.0016 mg/L from the original concentration. The removal efficiency was 96.55%, demonstrated that NMTB-200 performs well in practical application. Besides, considering the complexity of actual environmental water, future studies should evaluate the adsorption performance in wastewater with higher Cr(VI) concentrations and competing ions.

Table 2 compared the Cr(VI) adsorption capacity of NMTB with other biochars derived from tea residues and various agricultural/forestry wastes reported in recent literature. Despite the relatively low BET surface area of NMTB, it exhibited a competitive or superior adsorption capacity compared with most listed adsorbents. Compared with tea residue biochars prepared by conventional high-temperature pyrolysis, NMTB obtained by HTC achieved comparable removal efficiency (96.9%), with the additional advantages of lower synthesis temperature, no need for feedstock pre-drying, and simultaneous magnetization. This highlights the suitability of the hydrothermal route for processing wet tea waste. Moreover, waste tea residues have become a massively generated byproduct of the booming tea beverage industry, the selection of STL as the precursor provides a sustainable strategy about turning waste into adsorbent. It is both cost-effective and environmentally significant, which embodies the circular economy concept. It should be noted that the comparison is limited by differences in experimental conditions. Nevertheless, the overall trend demonstrates that NMTB stands out as a promising candidate for Cr(VI) removal, combining facile synthesis and competitive adsorption performance.

3.7 Adsorption mechanism investigation

3.7.1 FTIR and XPS analysis after adsorption

FTIR was employed to analyze the surface functional groups of magnetic biochars before and after adsorption, and the results were showed in Fig. 5c. It revealed that N and Fe elements were successfully doped onto the surface of all the NMTB samples, according to the peaks at 1060 cm^{-1} and 546 cm^{-1} representing C–N and Fe–O groups. Moreover,

Table 2 Comparative adsorption performance of Cr(VI) using various biochars

Biochar type	Preparation method	S_{BET} (m^2/g)	Adsorption condition		Adsorption capacity (mg/g)	Removal efficiency (%)	Reference
			pH	Initial Cr(VI) concentration (mg/L)			
Eucalyptus globulus bark	Pyrolysis, 2 h, 500 °C	265	2	20–40	21.3	/	[45]
Sugarcane bagasse	Pyrolysis, 2 h, 600 °C, magnetic biochar derived from steel pickling	29.918	4.63	/	43.122	/	[47]
Rice straw		33.850			33.227	/	
Peanut shells		36.791			13.579	/	
Herb residue		36.812			11.726	/	
Sugarcane bagasse	Hydrothermal carbonization, 12 h, 220 °C, HCl-activated	7.146	1	150	236.51	99.61%	[53]
Passion fruit peel	Hydrothermally treated, 7 h, 180 °C	12.08	2	175	35.68	/	[54]
Rice husk	Pyrolysis, 2 h, 500 °C, Fe-Zn-modified	134.6	2	10	9.97	/	[29]
Acacia falcata leaf powder	Hydrothermal carbonization, 15 h, 473 K, Fe-modified	6.83	2	40	36.15	/	[55]
Tea waste	Pyrolysis, 2 h, 450 °C	/	5.2	120	197.5	99.3%	[37]
Rice husk		/			195.24	96.8%	
Tea waste	Pyrolysis, 2 h, 450 °C, microwave post-modified	/	5.2	120	38.16	99.9%	[56]
Dried tea stalk	Pyrolysis, 2 h, 600 °C, Fe-modified	305.256	2	50	/	99.89%	[57]
Spent tea leaves	Hydrothermal carbonization, 4 h, 200 °C, Fe-N co-doped	21.335	2	50	63.03	96.9%	This work

after the adsorption of Cr(VI), the C=C/C=O and C–N vibrations of all three NMTB samples showed similar shift wavelengths, this may due to a redox reaction with Cr(VI), resulting in the reduction of Cr(VI) to Cr(III) and the subsequent formation of a precipitate [58]. The intensity of the characteristic peak at 546 cm^{-1} became weaker after adsorption, demonstrated that Fe–O group on the NMTBs surface participated the adsorption reaction. FTIR results indicated that the Cr(VI) adsorption process by NMTB involves both electrostatic attraction and chemical adsorption.

The surface composition and functional groups before and after adsorption were conducted by XPS analysis. It can be found from the wide scan of XPS spectrum (Fig. 5d) that the surface N and Fe contents were increased from 5.38 at.% and 2.77 at.% to 6.17 at.% and 3.47 at.%, respectively with the HTC temperature increased from 180 °C to 200 °C. Besides, a slight decrease of the surface N and Fe contents occurred when the HTC temperature increased from 200 °C to 220 °C, suggesting that the co-doped of N and Fe can enrich the surface functional groups of the biochars under appropriate HTC temperature [59, 60]. After adsorption, Cr2p peak can be observed on the surface of NMTBs, indicated that NMTBs had adsorbed a large amount of Cr (VI). The high resolution of Cr2p of NMTBs after adsorption presented in Fig. 5e. The peaks at around 577 eV and 586 eV are the characteristic peaks of Cr(III), which may resulting from the formation of Cr_2O_3, $FeCr_2O_4$, and $Cr(OH)_3$. Meanwhile, the peaks at around 579 eV and 588 eV are the characteristic peaks of Cr(VI) [61]. Based on the peak areas, it can be inferred that the Cr adsorbed on the NMTBs surface primarily exists in the form of Cr(III). The coexistence of Cr(VI) and Cr(III) on the NMTBs surface indicates that the valence state of surface Cr changes during the adsorption process; part of the Cr(VI) was reduced by the reducing agent to less toxic Cr(III) and adsorbed onto the biochars surface [62]. It can therefore be inferred that the removal mechanism of NMTBs for Cr(VI) primarily involves reduction and complexation, consistent with the results of FTIR analysis. The Fe2p spectrum (Fig. S5) of NMTBs exhibited that each sample can be separated into six divided peaks with the binding energy at around 711 and 724 eV were ascribed to Fe(II)$2p_{3/2}$ and Fe(II)$2p_{1/2}$, while peaks at around 713 and 726 eV that corresponded to Fe(III)$2p_{3/2}$ and Fe(III)$2p_{1/2}$, as well as their satellite peaks at 719 and 733 eV, respectively [22]. The Fe2p spectrum of NMTB presented the typical Fe(II) and Fe(III) spectrum, demonstrated the successful introduction of Fe into the biochars matrix. After adsorption, Fe(II) peaks area were increased suggested that Fe ion was involved in the adsorption reaction. This increase may be attributed to Cr coordinating with Fe–O active sites on the NMTB surface or to surface structural rearrangement, leading to a redistribution of electrons between Fe(II) and Fe(III). Therefore, XPS results supported that a chemical redox mechanism rather than pure physical adsorption of the Cr(VI) adsorption by NMTBs.

3.7.2 Zeta potential and point of zero charge analysis

Zeta potential measurements were conducted to evaluate the surface charge properties of NMTBs. As illustrated in Fig. 5f, the results demonstrated that with the increase of HTC temperature, NMTBs exhibited a slight increase of positive surface zeta potentials under acidic to neutral pH conditions (pH 3–7). Besides, the point of zero charge (pH_{PZC}) of NMTBs was slightly shifted from 4.41 (NMTB-180) to 5.31 (NMTB-220), which demonstrated the presence of metal oxide species and protonatable functional groups onto the biochar surface.

The initial pH of Cr(VI) solution can influence the potential charges of active sites present on the adsorbent. At low pH (when $pH < pH_{PZC}$), the surface of NMTBs is protonated and positively charged, favoring the electrostatic accumulation of anionic Cr(VI) species (such as $HCrO_4^-$ and $Cr_2O_7^{2-}$). Simultaneously, the reduction of Cr(VI) to Cr(III) is facilitated by the abundant H^+ ions, and the Fe dopant sites in NMTB serve as efficient electron donors under acidic conditions. With increasing pH, the surface charge changes, repelling the Cr(VI) anions, and the reduction reaction is kinetically inhibited, resulting in lower adsorption capacity (pH > 5). The observed trend of pH affection is consistent with the dominant mechanisms of electrostatic attraction and surface reduction.

In addition, by comparing the N1s spectrum before and after reaction (Fig. S6), the peaks of N species shift towards higher binding energy, suggesting the possibility of the coordination reaction between the doped N and Cr. The peak areas of graphite N increased, while those of pyrrolic N and pyridinic N decreased, which may due to the stronger coordination ability of pyrrolic N and pyridinic N with Cr(VI) ions. Therefore, the type of doped nitrogen is an important factor influencing the adsorption performance of Fe-NMBC These changes suggest the formation of coordination reaction between doped N and Cr [63]. The N-containing groups on NMTB undergo protonation at low pH, thus generate positively charged sites, which electrostatically attract the anionic Cr(VI) species ($HCrO_4^-$/$Cr_2O_7^{2-}$). As can be seen from the reaction, the subsequent reduction of Cr(VI) to Cr(III) consumes a large number of protons, promoting the removal of Cr(VI). The consumption of protons causes the solution pH to rise gradually as the reduction proceeds, which in turn lowers the redox potential of Cr(VI) and eventually limits further reduction. This is consistent with the high removal efficiency observed at acidic pH and the efficiency declined with the increase of pH. Generally,

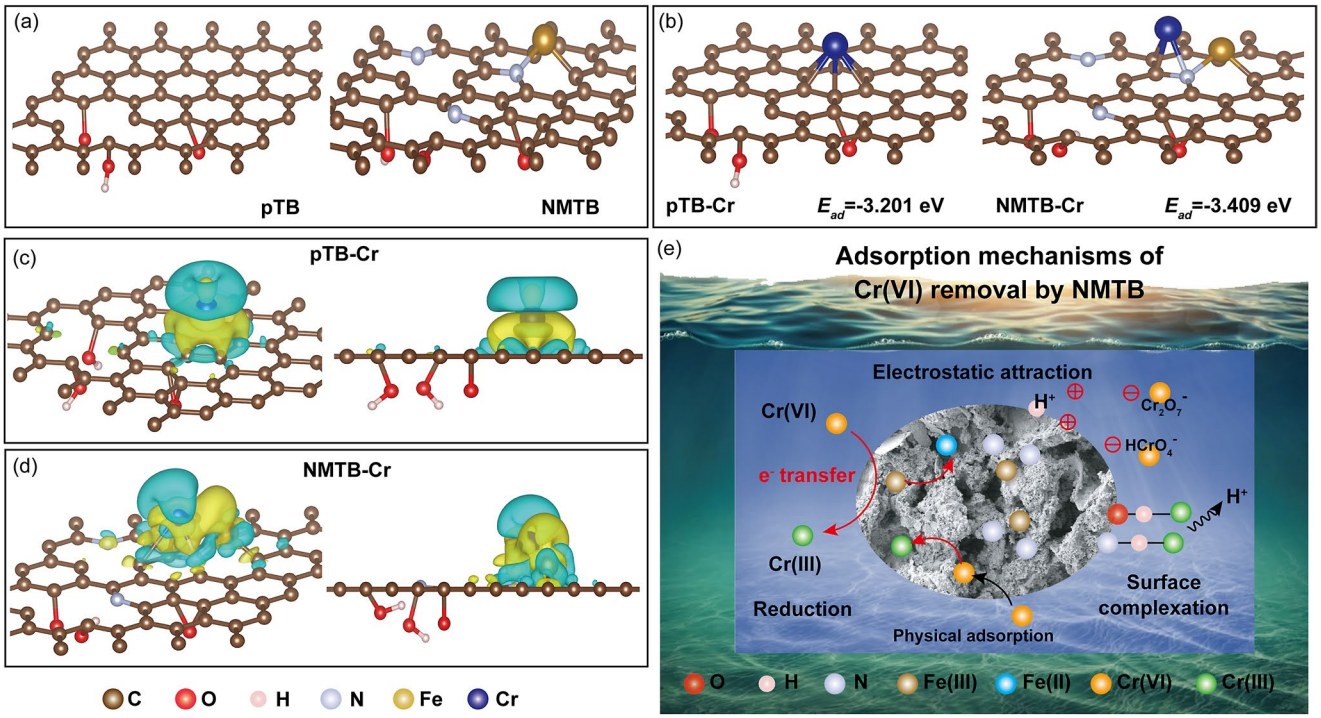

Fig. 6 The geometry structures of pTB and NMTB (**a**), diagram of the adsorption system and the adsorption energy of pTB and NMTB (**b**), top view and side view of the charge density difference of Cr adsorbed on pTB (**c**) and NMTB (**d**), and the adsorption mechanisms of Cr(VI) removal by NMTB (**e**). The different adsorption sites are referred to graphitic-N, pyrrolic-N, pyridine-N and Fe sites in (**b-d**). The cyan areas indicate electron-deficient regions and yellow areas indicate electron-concentrated regions in (**c-d**)

these findings confirm that electrostatic interaction plays an essential role in the initial accumulation of Cr(VI) on the NMTB surface prior to reduction and complexation.

3.7.3 Cr(VI)/Cr(III) distribution analysis during adsorption

To quantify the extent of Cr(VI) reduction, the distribution of Cr(VI) and Cr(III) in the solution after adsorption was analyzed. Specifically, the total Cr concentration was measured by ICP-OES, while the residual Cr(VI) concentration was determined by the spectrophotometric method. The Cr(III) concentration was then calculated as the difference between concentrations of total Cr and Cr(VI). Besides, the concentration of adsorbed Cr (Cr_{ADS}) on the solid phase can be calculated by subtracting the total Cr concentration in the solution after adsorption from the initial Cr concentration (50 mg/L). The results shown in Fig. 5g illustrated that total Cr concentrations was 20.65, 12.76 and 27.78 mg/L of NMTB-180, NMTB-200 and NMTB-220, respectively. Meanwhile, the Cr(VI) concentration decreased from an initial level of 50 mg/L to 12.92, 5.04 and 19.84 mg/L, respectively. Thus, Cr(III) concentrations were 7.73, 7.72 and 7.86 mg/L, respectively. It can be estimated that NMTB-180, NMTB-200 and NMTB-220 retained 29.35, 37.24 and 22.23 mg/L of Cr_{ADS} on the solid phase, respectively. NMTB-200 exhibited highest removal of Cr, with a minor fraction of the reduced Cr(III) released back into the solution (approximately 20%). It demonstrated that most of Cr(VI) was reduced to Cr(III) and subsequently immobilized on the NMTB surface, consistent with the findings of XPS analysis that Cr(III) are the dominant form of Cr2p. Together, these quantitative results confirmed that Cr(VI) removal proceeds predominantly by reduction and surface complexation of Cr(III) on the NMTB surface. Moreover, the applicability of the PSO kinetic model and the Langmuir model also indicated that the adsorption process is monolayer adsorption, in which chemical adsorption is the primary mechanism.

3.7.4 DFT calculation

In order to explore the adsorption mechanism theoretically, DFT calculations were performed to clarify the adsorption behavior of Cr (VI) on NMTB. According to the characterization results, the structure of Fe and N co-doped biochar (represent NMTB) was constructed using VASP 5.4.4 software, along with the original carbon structure substrate (represent pTB) for comparison (Fig. 6a). The computational details are described in Text S2 in Supplementary Material. Furthermore, the views of Cr adsorption on pTB and NMTB and their adsorption energies were presented in Fig. 6b. It can be seen from the absolute values perspective that the adsorption energy of Fe and N sites in NMTB was 3.409 eV,

which was superior to that of the corresponding sites in pTB (3.201 eV). This indicated that the synergistic effect of Fe and N in NMTB improved the adsorption performance of Cr, which is align with the adsorption capacity detected above. It has been reported that chemical adsorption is characterized by a relatively high absolute value of adsorption energy (>0.5 eV), which is typically negative [64]. In this work, the adsorption energy of NMTB (−3.409 eV) indicated that the adsorption of Cr by NMTB is dominated by a chemical adsorption process that significantly reduces the system's energy through the formation of chemical bonds. Figure 6c-d showed the top and side views of the charge density difference upon Cr adsorption of pTB and NMTB, respectively. The cyan areas in the Fig. 6c–d represent charge dissipation, while the yellow areas represent charge accumulation. It showed a clear charge transfer between Cr and the substrate, and this charge transfer is more pronounced in NMTB. Charge exchange also occurred between Fe and the substrate, resulting in increased substrate polarity and, consequently, increased adsorption energy between Cr and the substrate. There is a significant redistribution of charge density at the adsorption sites doped with Fe and N, suggested chemical adsorption of NMTB for Cr [65]. The DFT calculation demonstrated that chemical adsorption is the predominant adsorption mechanism and Fe and N dopants contribute to optimized the adsorption performance.

Based on the evidence presented above, the possible Cr (VI) removal mechanism by NMTB can be schematically illustrated in Fig. 6e. There are three main steps of the adsorption: (i) Electrostatic attraction. At the optimal pH of 2 (well below the pH_{PZC} of NMTB), negatively charged Cr(VI) species (such as $HCrO_4^-$ and $Cr_2O_7^{2-}$) are electrostatic attracted and accumulated on the surface of the biochar by the positive charge protonated on the surface of the biochar, as confirmed by zeta potential and pH_{PZC} analysis. (ii) Surface reduction. Once accumulated, Cr(VI) is reduced to Cr(III) by electron transfer from the active sites such as Fe and N dopant sites. This is supported by XPS detection of Cr(III) on the spent adsorbent surface, the quantitative distribution measurement that only a minor fraction of reduced Cr(III) released back into solution, and DFT calculation demonstrating a highly negative adsorption energy and direct electron transfer from the Fe dopant to Cr(VI). (iii) Surface complexation. The reduced Cr(III) is subsequently immobilized on the NMTB surface *via* complexation with functional groups, as evidenced by the shifts of N1s peaks in XPS and the changes in FTIR bands. The synergistic adsorption mechanism enables NMTB to effectively enrich Cr(VI) near the active sites and subsequently drive the reduction and complexation processes that reduced Cr(VI) to Cr(III), thus explain the high Cr(VI) uptake of NMTB despite its moderate surface area.

4 Conclusion

N-doped magnetic biochar derived from STL has been successfully produced through one-step HTC method with the modification of urea and $FeCl_3$. The results showed that the doping of N and Fe to the biochar significantly increased the specific surface area and Cr(VI) removal compared to pristine biochar. Moreover, optimization of the preparation process unveiled the highest removal efficiency of 96.90% under optimal preparation temperature and time of 200 °C and 4 h. NMTBs exhibited required suitable properties for Cr(VI) removal and the maximum adsorption capacity reached 63.03 mg/g by NMTB-200. Furthermore, monolayer sorption and chemisorption were the main adsorption process of NMTB. Reusability performance resulted in a removal efficiency of 84.49% after adsorption for five times, while removal rate in practical application was 96.55%. The removal mechanism demonstrated that electrostatic attraction is the initial driving force, where the surface is positively charged and hence facilitates the accumulation of anionic Cr(VI) species. Surface reduction plays the dominant role, which can be confirmed from the formation and quantitative of Cr(III) and DFT calculations. Shifts in XPS spectra and changes in FTIR bands suggested that surface complexation further immobilizes the reduced Cr(III). Overall, NMTB offers distinct advantages, including lower synthesis temperature, no need for feedstock pre-drying, one-step co-doping, and competitive adsorption efficiency. The valorization of STL from the rapidly expanding tea beverage industry is an effective, low-cost, and eco-friendly strategy for treating Cr(VI)-contaminated wastewater and aligns with circular economy principles.

Supplementary information The online version contains supplementary material available at https://doi.org/10.1007/s44442-026-00114-5.

Acknowledgements The authors extend their sincere gratitude to those who rendered assistance during the field investigation and sampling.

Author contributions Shasha Guo: Methodology, Formal analysis, Investigation, Data curation, Writing-original draft, Visualization, Funding acquisition. Pan Wang: Investigation, Writing-review and editing, Visualization. Yao Zhu: Conceptualization, Resources. Yinyin Zhou: Investigation, Data curation. Meiqin Li: Investigation, Resources. Xiao Lin: Investigation. Ping Xu: Conceptualization, Methodology, Writing-review and editing, Validation. Mufang Sun: Resources, Writing-review and editing, Funding acquisition.

Funding This work was supported and funded by the Science and Technology Project of Henan Province (252102111038), the Open Fund of Dabie Mountain Laboratory (DMLOF2024006), and the Natural Science Foundation of Henan Province(252300420728).

Data availability The data that support the findings of this study are available from the corresponding author upon reasonable request.

Declarations

Ethical approval Not applicable.

Competing interests The authors declare no competing interests.

References

1. Ton-That L, Nguyen TPT, Duong BN, Nguyen D-K, Nguyen N-A, Ho T, Dinh V-P (2024) Insights into Pb (II) adsorption mechanisms using jackfruit peel biochar activated by a hydrothermal method toward heavy metal removal from wastewater. Biochem Eng J 212:109525. https://doi.org/10.1016/j.bej.2024.109525
2. Chen J, Deng S, Jia W, Li X, Chang J (2021) Removal of multiple heavy metals from mining-impacted water by biochar-filled constructed wetlands: adsorption and biotic removal routes. Bioresource Technol 331:125061. https://doi.org/10.1016/j.biortech.2021.125061
3. Marella TK, Saxena A, Tiwari A (2020) Diatom mediated heavy metal remediation: a review. Bioresource Technol 305:123068. https://doi.org/10.1016/j.biortech.2020.123068
4. Qu J, Shi S, Li Y, Liu R, Hu Q, Zhang Y, Wang Y, Ma Y, Hao X, Zhang Y (2024) Fe/N co-doped magnetic porous hydrochar for chromium(VI) removal in water: adsorption performance and mechanism investigation. Bioresource Technol 394:130273. https://doi.org/10.1016/j.biortech.2023.130273
5. Elbasiouny H, Darwesh M, Elbeltagy H, Abo-Alhamd FG, Amer AA, Elsegaiy MA, Khattab IA, Elsharawy EA, Ebehiry F, El-Ramady H, Brevik EC (2021) Ecofriendly remediation technologies for wastewater contaminated with heavy metals with special focus on using water hyacinth and black tea wastes: a review. Environ Monit Assess 193(7):193449. https://doi.org/10.1007/s10661-021-09236-2
6. Liang H, Zhang H, Zhao P, Zhao X, Sun H, Geng Z, She D (2021) Synthesis of a novel three-dimensional porous carbon material and its highly selective Cr(VI) removal in wastewater. J Cleaner Prod 306:127204. https://doi.org/10.1016/j.jclepro.2021.127204
7. Mao X, Liu Y, Long S (2025) Research progress on adsorption mechanisms and regeneration applications of modified biochar for heavy metals in wastewater. Desalin Water Treat 324:101399. https://doi.org/10.1016/j.dwt.2025.101399
8. Meng K, Dong Y, Liu J, Xie J, Jin Q, Lu Y, Lin H (2025) Advances in selective heavy metal removal from water using biochar: a comprehensive review of mechanisms and modifications. J Environ Chem Eng 13(2):116099. https://doi.org/10.1016/j.jece.2025.116099
9. Hongthong S, Kankhwao P, Kohaeoklang S, Suwannahong K, Kreetachat T, Imman S, Suriyachai N, Dechapanya W, Dechapanya W, Phadee P, Wongcharee S (2026) Mitigating post-recycling plastic waste pollution through co-hydrothermal liquefaction with freshwater algal biomass: pathways to biofuel and high-value products as resource recovery: Chi River, Thailand. Sustainability 18(6):2962. https://doi.org/10.3390/su18062962
10. Jiang Y, Gao X, Sun K, Li C, Li B, Zhang S, Zhang L, Hu X (2025) Similarity and difference of biochar and hydrochar from leaves, bark, and wood of the same sycamore tree. Bioresource Technol 434:132778. https://doi.org/10.1016/j.biortech.2025.132778
11. Li Q, Jin Q (2025) Holistic comparison of hydrothermal carbonization versus slow pyrolysis for biochar production: techno-economic analysis and life cycle assessment. ACS Sustain Chem. Eng 13(31):12382–12395. https://doi.org/10.1021/acssuschemeng.5c02249
12. Chin JF, Heng ZW, Teoh HC, Chong WC, Pang YL (2022) Recent development of magnetic biochar crosslinked chitosan on heavy metal removal from wastewater – modification, application and mechanism. Chemosphere 291:133035. https://doi.org/10.1016/j.chemosphere.2021.133035
13. Mian MM, Liu G, Yousaf B, Fu B, Ullah H, Ali MU, Abbas Q, Mujtaba Munir MA, Ruijia L (2018) Simultaneous functionalization and magnetization of biochar via NH_3 ambiance pyrolysis for efficient removal of Cr (VI). Chemosphere 208:712–721. https://doi.org/10.1016/j.chemosphere.2018.06.021
14. Dobrzyńska J, Wysokińska A, Olchowski R (2022) Raspberry stalks-derived biochar, magnetic biochar and urea modified magnetic biochar - synthesis, characterization and application for As(V) and Cr(VI) removal from river water. J Environ Manag 316:115260. https://doi.org/10.1016/j.jenvman.2022.115260
15. Wu Y, Deng T, You X, Chen C, Chen Y, Hu X, Jin S, Yu X, Liu Z (2026) New-style tea beverages: integrating tea chemistry, matrix engineering, and intelligent systems toward consistent quality and scalability. Trends Food Sci Technol 175:105904. https://doi.org/10.1016/j.tifs.2026.105904
16. Ateş A, Mert Y, Timko MT (2023) Evaluation of characteristics of raw tea waste-derived adsorbents for removal of metals from aqueous medium. Biomass Conv Bioref 13(9):7811–7826. https://doi.org/10.1007/s13399-021-01721-5
17. Guo S, Awasthi MK, Wang Y, Xu P (2021) Current understanding in conversion and application of tea waste biomass: a review. Bioresource Technol 338:125530. https://doi.org/10.1016/j.biortech.2021.125530
18. Xing Y, Han Y, Li X, Fang L (2025) Modifier and pyrolysis optimization of algae-derived biochar enhances sulfamethoxazole removal via microalgae-biochar hybrids. Results Eng 28:108253. https://doi.org/10.1016/j.rineng.2025.108253
19. Guo X, Liu C, Lu F, Liu B, Zhang Q, Zhou T (2026) Preparation of a novel n-doped biochar from agricultural waste for Cu(II) removal: insights into the kinetic, equilibrium, adsorption mechanisms and economic feasibility. Water Air Soil Pollut 237(16):910. https://doi.org/10.1007/s11270-026-09592-0
20. Moon S, Lee YJ, Park SJ, Lee C-G (2024) Enhanced removal of micropollutants from water using $ZnCl_2$-modified *Spirulina* sp.-based biochar. J Appl Phycol 36(1):167–179. https://doi.org/10.1007/s10811-023-03122-9
21. Qu J, Liu Y, Meng J, Bi F, Ma S, Zhang G, Wang Y, Tao Y, Jiang Z, Zhang Y (2022) Pinecone-derived magnetic porous hydrochar co-activated by $KHCO_3$ and K_2FeO_4 for Cr(VI) and anthracene removal from water. Environ Pollut 306:119457. https://doi.org/10.1016/j.envpol.2022.119457
22. Cai B, Ouyang S, Fan J, Liu C, Zhang Y, Wei Z, Wang Z, Wang X, Lei H (2025) Preparation of highly-efficient Fe, N co-doping biochar from spent coffee grounds for the degradation of antibiotics

via Fenton-like reaction. J Environ Manag 388:126051. https://doi.org/10.1016/j.jenvman.2025.126051
23. Frindy S, Sillanpää M (2020) Synthesis and application of novel α-Fe_2O_3/graphene for visible-light enhanced photocatalytic degradation of RhB. Mater Des 188:108461. https://doi.org/10.1016/j.matdes.2019.108461
24. Zhao J, Shen XJ, Domene X, Alcañiz J-M, Liao X, Palet C (2019) Comparison of biochars derived from different types of feedstock and their potential for heavy metal removal in multiple-metal solutions. Sci Rep 9(1):9869. https://doi.org/10.1038/s41598-019-46234-4
25. Jaiswal KK, Kumar V, Verma R, Verma M, Kumar A, Vlaskin MS, Nanda M, Kim H (2021) Graphitic bio-char and bio-oil synthesis *via* hydrothermal carbonization-co-liquefaction of microalgae biomass (oiled/de-oiled) and multiple heavy metals remediations. J Hazard Mater 409:124987. https://doi.org/10.1016/j.jhazmat.2020.124987
26. Zhu H, Zhang R, Zhang Z, Tan B, Chen D (2026) Synergistic catalysis of graphitic N and carbonyl groups in N-doped biochar for peroxymonosulfate activation toward non-radical tetracycline degradation. Colloids Surf A 734:139413. https://doi.org/10.1016/j.colsurfa.2025.139413
27. Shan C, Ma Z, Tong M (2014) Efficient removal of trace antimony(III) through adsorption by hematite modified magnetic nanoparticles. J Hazard Mater 268:229–236. https://doi.org/10.1016/j.jhazmat.2014.01.020
28. Mei Y, Xu J, Zhang Y, Li B, Fan S, Xu H (2021) Effect of Fe–N modification on the properties of biochars and their adsorption behavior on tetracycline removal from aqueous solution. Bioresource Technol 325:124732. https://doi.org/10.1016/j.biortech.2021.124732
29. Sinha R, Kumar R, Abhishek K, Shang J, Bhattacharya S, Sengupta S, Kumar N, Singh RK, Mallick J, Kar M, Sharma P (2022) Single-step synthesis of activated magnetic biochar derived from rice husk for hexavalent chromium adsorption: equilibrium mechanism, kinetics, and thermodynamics analysis. Groundwater Sust Dev 18:100796. https://doi.org/10.1016/j.gsd.2022.100796
30. Mondal AK, Hinkley C, Kondaveeti S, Vo PHN, Ralph P, Kuzhiumparambil U (2024) Influence of pyrolysis time on removal of heavy metals using biochar derived from macroalgal biomass (*Oedogonium* sp.). Bioresour Technol 414:131562. https://doi.org/10.1016/j.biortech.2024.131562
31. Wang Z, Liu K, Xie L, Zhu H, Ji S, Shu X (2019) Effects of residence time on characteristics of biochars prepared via co-pyrolysis of sewage sludge and cotton stalks. J Analytical Appl Pyrolysis 142:104659. https://doi.org/10.1016/j.jaap.2019.104659
32. Liu J, Zhu J, Gao Q, Zeng X, Zeng Q, Xiong J, Zhang G, Niu Y, Xie H (2025) Accelerate degradation of tetracycline via persulfate activation over S, N-Fe co-doped banana peel biochar: the role of pyrolysis temperature and $1O_2$ evolution. Chem Eng J 509:161425. https://doi.org/10.1016/j.cej.2025.161425
33. Hu C, Ding X, Zhao Z, Zhang S, Wei Q, Zhang H, Zhang Y, Deng B, Pan M, Mei Y (2026) Efficient removal of Cu(II) from wastewater using novel *Ginkgo biloba* leaf-based magnetic biochar composites: performance, mechanism, and repeatability evaluation. J Environ Chem Eng 14(1):121146. https://doi.org/10.1016/j.jece.2026.121146
34. Maisyarah S, Ahmed MMM, Tseng KM, Hsu L-C, Venkatesan S, Hsieh Y-C, Hsieh J, Tzou Y-M, Jien S-H (2025) Magnetically recoverable iron-modified biochar for high-efficiency phosphate separation: process optimization and DFT-validated mechanisms. Separat Purif Technol 379:135171. https://doi.org/10.1016/j.seppur.2025.135171
35. Mishra A, Kaur L, Sharma M, Sharma P, Murab S, Ojha H, Pandey J, Pathak M (2025) Magnetic biochar from marigold floral waste: synthesis, characterization, and adsorptive removal of methylene blue. J Mol Struct 1341:142657. https://doi.org/10.1016/j.molstruc.2025.142657
36. Zhang M, Liu G, Liu R, Xu J, Si W, Wei Y (2024) High-efficient co-removal of copper and zinc by modified biochar derived from tea stalk: characteristics, adsorption behaviors, and mechanisms. J Water Process Eng 57:104533. https://doi.org/10.1016/j.jwpe.2023.104533
37. Khalil U, Shakoor MB, Ali S, Rizwan M, Nasser Alyemeni M, Wijaya L (2020) Adsorption-reduction performance of tea waste and rice husk biochars for Cr(VI) elimination from wastewater. J Saudi Chem Soc 24(11):799–810. https://doi.org/10.1016/j.jscs.2020.07.001
38. Ghorbani-Khosrowshahi S, Behnajady MA (2016) Chromium(VI) adsorption from aqueous solution by prepared biochar from Onopordom Heteracanthom. Int J Environ Sci Technol 13(7):1803–1814. https://doi.org/10.1007/s13762-016-0978-3
39. Zou C, Xu Z, Nie F, Guan K, Li J (2023) Application of hydroxyapatite-modified carbonized rice husk for the adsorption of Cr(VI) from aqueous solution. J Mol Liq 371:121137. https://doi.org/10.1016/j.molliq.2022.121137
40. Wang S, Tang Y, Li K, Mo Y-Y, Li H-F, Gu Z-Q (2014) Combined performance of biochar sorption and magnetic separation processes for treatment of chromium-contained electroplating wastewater. Bioresource Technol 174:67–73. https://doi.org/10.1016/j.biortech.2014.10.007
41. Li K, Hanpei Y, Lina W, Siqi C, Ruichen Z, Junming W, Xiaona L (2020) Facile integration of FeS and titanate nanotubes for efficient removal of total Cr from aqueous solution: synergy in simultaneous reduction of Cr(VI) and adsorption of Cr(III). J Hazard Mater 398:122834. https://doi.org/10.1016/j.jhazmat.2020.122834
42. Guo N, Lv X, Yang Q, Xu X, Song H (2021) Effective removal of hexavalent chromium from aqueous solution by $ZnCl_2$ modified biochar: effects and response sequence of the functional groups. J Mol Liq 334:116149. https://doi.org/10.1016/j.molliq.2021.116149
43. Zhang L, Tang S, Jiang C, Jiang X, Guan Y (2018) Simultaneous and efficient capture of inorganic nitrogen and heavy metals by polyporous layered double hydroxide and biochar composite for agricultural nonpoint pollution control. ACS Appl Mater Interfaces 10(49):43013–43030. https://doi.org/10.1021/acsami.8b15049
44. Jeyaseelan C, Gupta A (2020) Green tea leaves as a natural adsorbent for the removal of Cr(VI) from aqueous solutions. Air Soil Water Res 9. https://doi.org/10.1177/ASWR.S35227
45. Choudhary B, Paul D (2018) Isotherms, kinetics and thermodynamics of hexavalent chromium removal using biochar. J Environ Chem Eng 6(2):2335–2343. https://doi.org/10.1016/j.jece.2018.03.028
46. Ma F, Zhao B, Diao J (2019) Synthesis of magnetic biochar derived from cotton stalks for the removal of Cr(VI) from aqueous solution. Water Sci Technol 79(11):2106–2115. https://doi.org/10.2166/wst.2019.208
47. Yi Y, Tu G, Zhao D, Tsang PE, Fang Z (2019) Biomass waste components significantly influence the removal of Cr(VI) using magnetic biochar derived from four types of feedstocks and steel pickling waste liquor. Chem Eng J 360:212–220. https://doi.org/10.1016/j.cej.2018.11.205
48. Sinha R, Kumar R, Sharma P, Kant N, Shang J, Aminabhavi TM (2022) Removal of hexavalent chromium via biochar-based adsorbents: state-of-the-art, challenges, and future perspectives. J Environ Manag 317:115356. https://doi.org/10.1016/j.jenvman.2022.115356
49. Langmuir I (1918) The adsorption of gases on plane surfaces of glass, mica and platinum. J Am Chem Soc 40(9):1361–1403. https://doi.org/10.1021/ja02242a004

50. Bulut E, Özacar M, Şengil İA (2008) Adsorption of malachite green onto bentonite: equilibrium and kinetic studies and process design. Microporous Mesoporous Mater 115(3):234–246. https://doi.org/10.1016/j.micromeso.2008.01.039
51. Tan X, Liu Y, Zeng G, Wang X, Hu X, Gu Y, Yang Z (2015) Application of biochar for the removal of pollutants from aqueous solutions. Chemosphere 125:70–85. https://doi.org/10.1016/j.chemosphere.2014.12.058
52. Lee EJ, Lee JW (2025) Dual adsorption–reduction mechanism of alginate-immobilized magnetic biochar beads for Cr(VI) removal. Environ Technol Innovation 40:104660. https://doi.org/10.1016/j.eti.2025.104660
53. Yang M, Lu R, Wei Y, Guo Y, Lan L, Lu J, Liao Y, Li H, Lan P, Kou Z (2025) Preparation of highly functionalised biochar from hydrochloric acid activated bagasse for the efficient removal of metal ions. Process Saf Environ Protect 195:106736. https://doi.org/10.1016/j.psep.2024.12.117
54. Yuzhu Z, Hua L, Sihua Z (2026) Upcycling waste passion fruit peel into carbon dots and biochar via one-pot hydrothermal synthesis for dual Cr(VI) sensing and removal. Biomass Conv Bioref 16(10):233. https://doi.org/10.1007/s13399-026-07154-2
55. Juturu R, Selvaraj R, Murty VR (2024) Efficient removal of hexavalent chromium from wastewater using a novel magnetic biochar composite adsorbent. J Water Process Eng 66:105908. https://doi.org/10.1016/j.jwpe.2024.105908
56. Shakoor MB, Khalil U, Ali S, Sharif F, Ahmad SR, Rizwan M, Jilani A, Al-Ghanim KA, Sarker PK (2024) Microwave-assisted magnetic biochar for removal of hexavalent chromium from aqueous solution. Environ Pollutants Bioavailability 36(1):2368590. https://doi.org/10.1080/26395940.2024.2368590
57. Mao Y, Tao Y, Zhang X, Chu Z, Zhang X, Huang H (2023) Removal of aqueous Cr(VI) by tea stalk biochar supported nanoscale zero-valent iron: performance and mechanism. Water Air Soil Pollut 234(3):149. https://doi.org/10.1007/s11270-023-06164-4
58. Cheng W, Ding C, Wang X, Wu Z, Sun Y, Yu S, Hayat T, Wang X (2016) Competitive sorption of As(V) and Cr(VI) on carbonaceous nanofibers. Chem Eng J 293:311–318. https://doi.org/10.1016/j.cej.2016.02.073
59. Guo L, Lai X, Peng L, Li J, Zhang W, Shi B (2023) Facile synthesis of Fe and N co-coped biochar from low temperature pyrolysis of lignin waste for superefficient Th(IV)/U(VI) separation: performance and mechanism. J Cleaner Prod 426:139168. https://doi.org/10.1016/j.jclepro.2023.139168
60. Mao XY, Liu YL, Cao CY, Wang H, Wang S, Zhao Y-H (2026) Orange peel-derived iron-doped biochar for efficient and rapid Fenton-like degradation of Rhodamine B: role of temperature-induced iron species evolution. J Water Process Eng 83:109577. https://doi.org/10.1016/j.jwpe.2026.109577
61. Wu L, Liao L, Lv G, Qin F, He Y, Wang X (2013) Micro-electrolysis of Cr (VI) in the nanoscale zero-valent iron loaded activated carbon. J Hazard Mater 254-255:277–283. https://doi.org/10.1016/j.jhazmat.2013.03.009
62. Zhang L, Fu F, Tang B (2019) Adsorption and redox conversion behaviors of Cr(VI) on goethite/carbon microspheres and akaganeite/carbon microspheres composites. Chem Eng J 356:151–160. https://doi.org/10.1016/j.cej.2018.08.224
63. Zhou J, He Y, Wang J, He G, Wang C, Huang L, Zhao Y, Feng G (2026) Mechanical activation coupled pyrolysis prepares Fe/N-doped macadamia biochar: dual-function sites enable synergistic Cr(VI) adsorption and reduction. J Ind Eng Chem 154:822–834. https://doi.org/10.1016/j.jiec.2025.10.053
64. Yin Q, Gao Y, Wang R, Zhu X, Gao X, Zhao Z, Li J, Ma K (2026) Influence of Fe-N co-doping on biochar on the adsorption of CO_2. Chem Eng Sci 320:122702. https://doi.org/10.1016/j.ces.2025.122702
65. Huo S, Ni W, Zhao Y, Song X, Zhao Y, Li K, Wang H, Zhang M (2021) Highly efficient atomically dispersed Co–N active sites in porous carbon for high-performance capacitive desalination of brackish water. J Mater Chem A 9(5):3066–3076. https://doi.org/10.1039/D0TA10886C